Behaviour of Orthogonal Wave Functions And The Correction of Antenna Measurements Taken in Non-Anechoic Environments

S.F. Gregson, A.C. Newell, G.E. Hindman
Nearfield Systems Inc.
19730 Magellan Drive
Torrance, CA, 90502, USA

***Abstract*—The measurement and post-processing mode orthogonalisation and filtering technique, named Mathematical Absorber Reflection Suppression (MARS) [1, 2], has been used extensively to identify and subsequently extract measurement artefacts arising from spurious scattered fields that are admitted when antenna testing is performed in non-ideal anechoic environments. Underpinning the success of the MARS post-processing, and other mode orthogonalisation and filtering strategies [3], is the behaviour of the orthogonal vector wave (mode) expansions that are employed to describe the radiated fields and in particular their behaviour under the isometric co-ordinate translations that are central to the post processing. Within this paper, simulated and measured data will be used to illustrate the applicability of this measurement and post processing technique paying particular attention to the behaviour of the various modal expansions examining and confirming specific, commonly encountered, measurement conventions.**

Keywords— Antenna measurements; multipath suppression; spherical mode expansion; mode orthogonalisation; mode filter; MARS

I. INTRODUCTION

In many instances, the integrity of an antenna measurement can be compromised in a large part by range reflections, *i.e.* clutter, which is often found to constitute one of the largest contributors to the overall facility level error budget [4]. Typically, when taking antenna measurements indoors, spurious scattered field are significantly attenuated by covering the interior of the chamber and much of the measurement equipment with RF absorbing material (RAM). This material, is typically manufactured using open-cell Carbon impregnated foam, can be bulky, costly, fragile, and over time often the particles of Carbon can be released in the form of dust. Most absorber is optimised so that its performance is tailored for use across a predetermined range of frequencies with some performance degradation outside of that band. Thus, this material is not perfectly matched to illuminating fields for all directions, polarisations and frequencies, with the impedance mismatch inevitably resulting in some degree of scattering. Furthermore, whilst considerable effort can be devoted to optimising the placement of this RAM material within the range, this material cannot be installed everywhere and generally linear bearings, lights, fire detection and suppression equipment, *etc.* are left exposed.

Although many scattering suppression methods have been tested with examples including: time-gating (both hardware and software), spatial filtering, RF subtraction, parametric repeat measurement, and waveform correlation; it is only recently generalised mode filtering and orthogonalisation based technique, named Mathematical Absorber Reflection Suppression (MARS), has become available for use with *all* forms of near- and far-field antenna range testing. MARS is a frequency domain measurement and post-processing technique that has been successfully employed to reduce range multi-path effects within spherical [1, 2], cylindrical [5], plane-rectilinear [6], plane-polar [7] near-field test systems; as well with far-field [8], single parabolic [9], and dual cylindrical reflector [10] compact antenna test ranges (CATR). The effectiveness of the MARS technique has been attested to through the use of computational electromagnetic simulation [10, 11] and actual range measurement, across a wide frequency range stretching from UHF to mm-wave frequencies, with significant benefits being brought to measurements of low to high directive gain, linear and circularly polarised antennas with meaningful results even be being obtained from systems containing limited or no absorber.

Examination of the implementation of the aforementioned variants of MARS, and any other similar technique *e.g.* [12], reveal that each and every implementation is predicated upon the successful application of a modal expansion, a translation of origins, and a modal filtering algorithm. Thus, it is clear that the underlying MARS technique is not merely a "peculiarity" of one particular modal basis or sampling scheme, *etc.* but is a far more general principle that allows a distinction to be drawn between the field emanating from an antenna and the field arising from range clutter, that is independent of the particular mathematical treatment being utilised. Below, Section II summarises the spherical implementation of MARS, Section III introduces the computational electromagnetic (CEM) model before Section IV examines the critical behaviour of the orthogonal wave functions in relation to the range measurement through numerical modelling.

II. OVERVIEW OF SPHERICAL MARS

From electrodynamics it is well know that any given free-space electromagnetic field can be constructed from a linear superposition of any complete set of valid basis functions

978-1-4799-0091-6/13/$31.00

where these modes are exact analytic solutions of Maxwell's equations. Standard spherical near-field theory is based on the transmission equation derived by Jensen [13, 14] and further developed by Wacker [15] where the antenna under test and the probe are described by spherical mode coefficients that are the coefficients of basis functions that are solutions of Maxwell's equations for a spherical co-ordinate system. In principle, the transmission equation is valid for any arbitrary test antenna and probe combination at any separation distance between the spherical co-ordinate system origin and the probe that is outside of the minimum sphere of radius ρ_0 that will completely enclose the majority of the current sources. A linear isotropic and homogeneous source or sink free space which is enclosed by a spherical surfaces and which is located at the origin of an inertial frame of reference, the electric field can be written as [14],

$$\underline{E}(r,\theta,\phi) = k_0\sqrt{Z}\sum_{n=1}^{\infty}\sum_{m=-n}^{n}\left[Q_{TEmn}^{(3)}\underline{F}_{TEmn}^{(3)}(r,\theta,\phi) + Q_{TMmn}^{(3)}\underline{F}_{TMmn}^{(3)}(r,\theta,\phi)\right] \quad (1)$$

Here, $Q_{TMmn}^{(3)}$ and $Q_{TEmn}^{(3)}$ denote the transverse magnetic (TM) and transverse electric (TE) spherical mode coefficients, which are complex values of n and m, $\underline{F}_{TMmn}^{(3)}$ and $\underline{F}_{TEmn}^{(3)}$ are TM and TE spherical vector wave-functions which are functions of n, m, r, θ, ϕ. Here, spherical Hankel functions are used to represent radial outgoing waves. The spherical mode coefficients (SMC) are complex numbers that are functions of frequency, the polarization index, the polar index n, and the azimuthal index m such that $0 \le n \le \infty$ and $-n \le m \le n$ which do not vary with any of the scanning co-ordinates. The study of the behaviour of these coefficients is the central theme of this paper. The summation can in practice not be infinite and instead the maximum value for the polar summation is truncated to a finite integer number which is large enough to enable the field to be precisely and accurately and represented. Thus, it is assumed that the antenna under test (AUT) is enclosed within a sphere of radius ρ_0 (maximum radial extent) that is centred on the origin of the measurement co-ordinate system, spherical waves of order $N > k_0\rho_0$ represent the most complex constituents of the field structure thus typically N is chosen so that [14],

$$N = \text{ceil}(k_0\rho_0) + n_1 \quad (2)$$

Here, ceil is used to denote a function that rounds to the nearest integer towards positive infinity, and n_1 is a positive integer that depends upon the accuracy required (*e.g.* $n_1 = 10$). In order to be able to perform the integration for the angular variables using incrementally measured data, the data point spacing for all angles must satisfy the sampling criteria for each variables. Theoretical guidelines are available to specify the angular spacing in θ and ϕ in terms of the radius of the minimum sphere that will completely enclose the antenna. Although a detailed mathematical treatment of the MARS processing is left to the open literature [1, 2, 5, 6, 7, 8, 9], an overview of the generic MARS processing algorithm is summarized below as this is used in the subsequent sections:

1. Acquire two orthogonal tangential near electric field components. Solve for the TE and TM mode coefficients.
2. Deduce the unknown test antenna mode coefficients using probe pattern mode coefficients that have been computed a priori.
3. Use the inverse procedure to calculate the asymptotic far electric field from probe compensated spherical modes.
4. Mathematically translate the test antenna to the origin of the measurement co-ordinate system.
5. Re-compute the not ideally located test antenna from the far electric fields.
6. Use a modal filter to attenuate spurious higher order modes.
7. Calculate the MARS filtered far-field pattern from the filtered mode coefficients.

Fig. 1. NSI-RF-WR284 OEWG probe being tested at NSI on NSI-700S-90 in open factory environment with no anechoic chamber.

To illustrate the effectiveness of the MARS measurement and post-processing a NSI-RF-WR284 open-ended rectangular waveguide (OEWG) probe was acquired on an NSI-700S-90 overhead scanning arm spherical near-field test system at two different Z distances from the θ and ϕ axis intersection in an open factory setting. That is to say, in an environment with a large level of range reflection, *i.e.* clutter (also, note that although partially fabricated from dielectric much of the spherical positioning system was not covered in RF absorber). This "θ over ϕ" type spherical test system can be seen presented in Figure 1 below. OEWG probes are low gain devices, typically ~6 dBi, and as such tend to illuminate sidewalls, *etc*., with relatively large levels of radiation thereby becoming susceptible to the effects of range reflections.

The resulting far-field pattern was calculated at 2.6 GHz without applying MARS processing. These results are shown in Figure 2, where they are compared to an equivalent result that was obtained using a reference spherical system that was sited within a conventional anechoic chamber. The patterns on the open range are clearly quite different due to the very poor reflection environment. Conversely, applying the MARS processing yields the comparison in Figure 3 where it can be seen that the measurements from the open range are in very good agreement with those from the conventional anechoic chamber. During this campaign it was noted that additional benefit was obtained by doubling the sampling rate a point that is examined in more detail in the following section. Although the MARS measurement set out above constitutes a fairly extreme case, these results *are* typical of the sorts of improvement that can be attained with this measurement and post-processing technique, and they represent a good configuration to model using a CEM simulation. This numerical model is introduced in the following section.

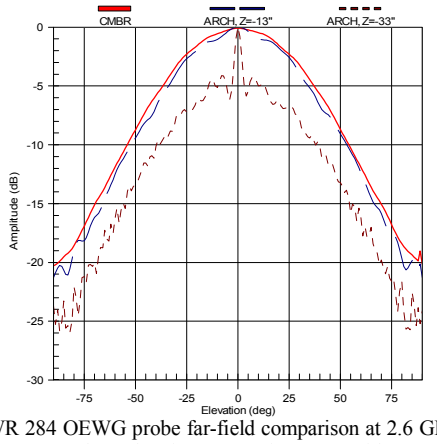

Fig. 2. WR 284 OEWG probe far-field comparison at 2.6 GHz of chamber measured data, versus data taken in open environment without MARS.

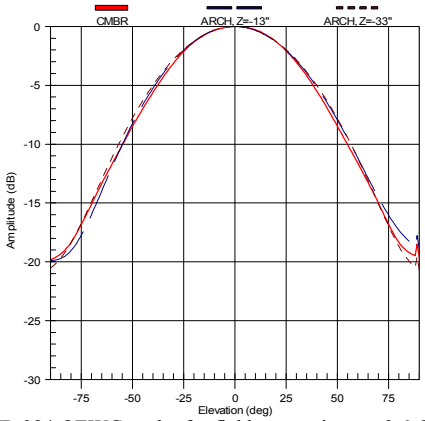

Fig. 3. WR 284 OEWG probe far-field comparison at 2.6 GHz of chamber measured data, versus data taken in open environment with MARS.

III. Overview Of Spherical MARS Simulation

In order that the behaviour of the SMC under MARS processing could be illustrated and examined in the absence of the ingress of other spurious measurement errors, the use of a simple computational simulation was harnessed. A numerical approach was sought as analytical verification techniques are complicated by the difficulty with which closed form solutions can be obtained for complex configurations such as those inherent to the MARS measurement. Furthermore, even when exact solutions are available, they tend to be cumbersome and difficult to use. The elementary (Hertzian) dipole has a closed form expression that is valid everywhere (*i.e.* in the both the near, *and* far-field) except at the dipole itself. In addition, formulas are available for an arbitrarily orientated and arbitrarily located dipole located in a homogeneous medium [16]. A linear superposition of dipoles, with due regard to phase, can be used to simulate far more complex radiating structures providing great flexibility [17]. The inclusion of an arbitrarily located perfectly conducting (*i.e.* worst case) scattering object can be easily introduced by harnessing image theory [18]. This method implies virtual (*i.e.* not real) sources are introduced in combination with the real sources form an equivalent system that replaces the actual system above the conductor. This arrangement is shown in Figure 4 below. As the dipole is vertically polarised, that is to say it is aligned with the surface normal to the perfect electric conductor (PEC) surface, the normal component of the electric field remains unchanged upon reflection (*c.f.* tangential component would be reversed in sign) [19]. Using this elementary model, it is possible to recreate the θ over ϕ spherical near-field (SNF) measurement configuration shown above in Figure 1. Results of the use of this simulation are presented in the following section.

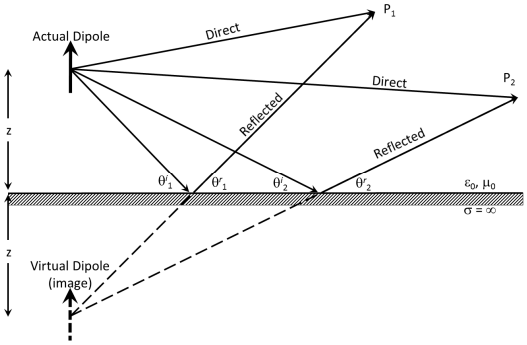

Fig. 4. Vertical dipole and its reflected image for a flat perfectly conducting surface of infinite extent for two SNF measurement positions.

IV. Preliminary Results of CEM Simulation

In order that the CEM simulation could be tested, the fields of a Hertzian dipole radiating at 10 GHz were simulated over the surface of an acquisition sphere at a radius of 50 wavelengths. These fields were then transformed from the finite (r = 50λ) far-field to the asymptotic far-field using a standard spherical near-field to far-field transform [13, 14, 15]. For a dipole when r is larger than a few wavelengths the field point can be considered to be in the far-field. These fields were then resolved onto a Ludwig II azimuth over elevation polarisation basis and tabulated on a regular azimuth over elevation co-ordinate system [20]. These far-field patterns can be seen presented in the form of false colour checkerboard plots in Figures 5 and 6 below. As expected the finite range far-field (not shown) and true far-field amplitude and phase patterns were in excellent agreement.

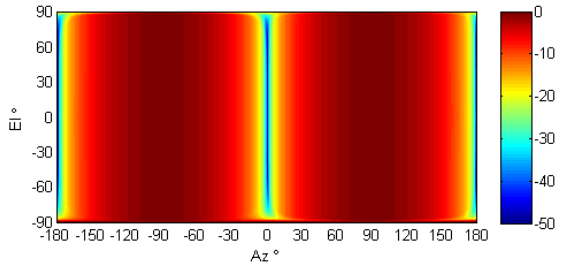

Fig. 5. E_{Az} Polarised far electric field component of Hertzian dipole.

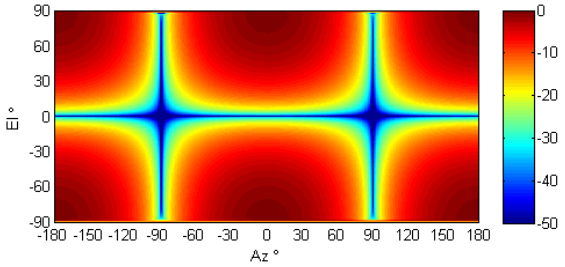

Fig. 6. E_{El} Polarised far electric field component of Hertzian dipole.

In the absence of other experimental errors, merely displacing an antenna from the origin of the spherical

measurement co-ordinate system will have no effect on the far-field amplitude pattern although it will result in the introduction of a phase taper on the far-field phase function [5, 6]. Such an offset in the near-field measurement between the AUT and the probe causes the phase of the measured signals to vary more rapidly across the acquisition surface and produce a broad distribution of modes. This effect can be seen illustrated in Figures 7, 8, 9, and 10 which contain false colour (checkerboard) plots of the amplitudes of the TM SMCs which were obtained from a Hertzian dipole as it was progressively displaced away from the origin of the measurement co-ordinate system by 1λ, 5λ and 10λ in the *x*- and *z*-axes respectively with the modes having been plotted as functions of the polar and azimuthal mode indices. Figure 7 represents the TM SMC for the case where the Hertzian dipole was located at the origin and as such only a single $m = n = 1$ mode is needed to represent the complete radiated field distribution. This behaviour is expected and consistent with equation (2). In each of these plots, modes for which $|m| > n$ are (mathematically) undefined and have been represented with white space. Although transverse electric (TE) and transverse magnetic (TM) spectra are in general needed to uniquely determine the field, as the Hertzian dipole was aligned with the *z*-axis; only the corresponding, *i.e.* dominant, TM polarised mode spectra have been plotted here.

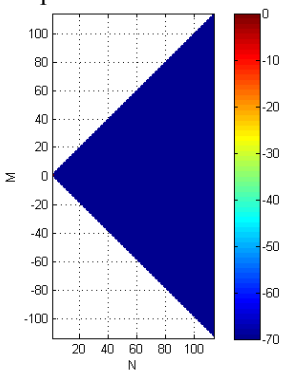

Fig. 7. TM SMCs for dipole at origin (a single lowest order mode).

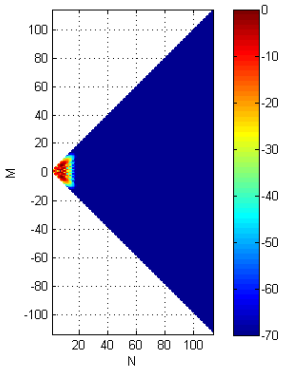

Fig. 8. TM SMCs for dipole when displaced by $x = z = 1\lambda$.

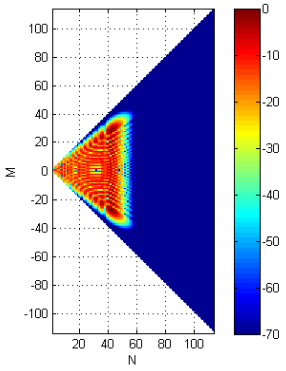

Fig. 9. TM SMCs for dipole when displaced by $x = z = 5\lambda$.

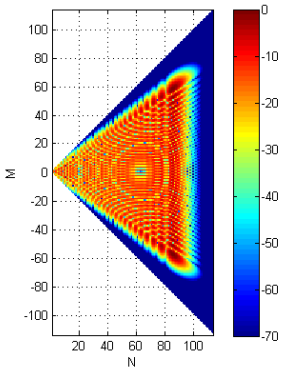

Fig. 10. TM SMCs for dipole when displaced by $x = z = 10\lambda$.

Thus, although the respective mode distributions vary markedly between these simulations, it is crucial to note that the respective far-field amplitude patterns (principal and cross-polarised, axial ratio, gain, directivity, *etc*.) are exactly the same in every case. To investigate the effect of MARS processing on the SMCs, a further simulation was performed however in this case the dipole was located coaxially (*i.e.* $x = y = 0$) at $z = 7.5\lambda$ away from the origin. As the Hertzian dipole was aligned with the *z*-axis, and as the offset was also in the *z*-axis, only the TM SMCs were needed with the TE SMCs being more than 300 dB below the largest TM SMC. Also, as the dipole was coaxial to the spherical co-ordinate system, only the mode indices for which $M = 0$ were needed. The amplitude for these modes can be seen plotted in Figure 11 below. As the offset was 7.5λ using equation (2), this implies that $N_{max} = 15\pi + 10 \sim 57$. Here, it is clear that the $N = 57$ mode is *circa* 60 dB below the largest SMC thereby verifying equation (2) for this simple case. Similarly, Figure 12 contains an equivalent plot for the virtual (image) dipole. This dipole is electrically equivalent to the real dipole only by applying the theory of images, it has been situated at $z = -7.5\lambda$. From inspection of Figures 11 and 12 it is clear that the amplitude spectra for the real and virtual dipoles are identical, with differences only manifesting themselves within the phases of the respective mode coefficient.

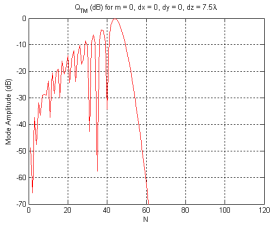

Fig. 11. Mode spectra for dipole located coaxially at $z = 7.5\lambda$

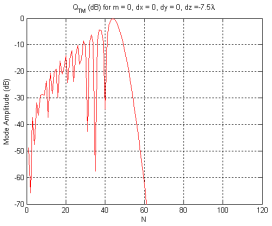

Fig. 12. Mode spectra for "virtual" dipole located coaxially at $z = -7.5\lambda$.

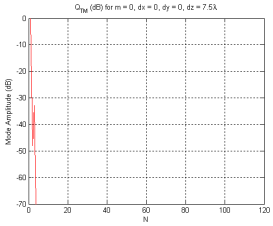

Fig. 13. Mode spectra for dipole located coaxially at $z = 7.5\lambda$ having been translated by -7.5λ to $z = 0$.

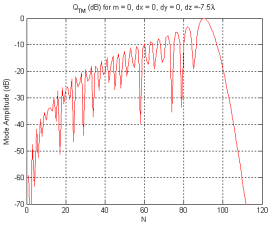

Fig. 14. Mode spectra for "virtual" dipole located coaxially at $z = -7.5\lambda$ having been translated by -7.5λ to $z = -15\lambda$.

As detailed above in Section II, the MARS post processing algorithm requires the application of a translation of origins. This mathematical operation is intended to reposition the AUT at the origin of the measurement co-ordinate system. So as to illustrate the effect that this has on the corresponding SMCs, Figure 13 contains a plot of the amplitude of the $m = 0$ TM mode coefficients after this translation of origins has been applied. Here it is clear that, as expected, only a very small number of SMCs are required to represent the Hertzian dipole with all but the first few modes being more than 70 dB below the largest mode amplitude. Figure 14 contains an equivalent mode plot for the "virtual" dipole. As this dipole was initially situated at $z = -7.5\lambda$, if one were to apply the same translation as was used for the "real" dipole then this would result in the virtual dipole being translated to $z = -15\lambda$. From equation (2) this would imply that this current source would require a larger number of SMCs to reconstruct its field. From inspection of Figure 14 this is exactly what can be seen with the highest order mode increasing from ~ 57, *c.f.* Figure 12, to $N_{max} = 30\pi$

+ 10 ~ 105. Note also, as the centre of the distribution of SMCs increases, correspondingly, the amount of power contained within the lowest order mode decreases. This translation of SMCs supports the often stated additional MARS requirement of sampling the data at twice the normal density. This can be interpreted as resulting from the need to insure these higher order modes which are associated with scattered fields are not aliased back onto the pattern modes through cyclic convolution during the modal expansion.

As set out in the previous section, it is possible to create a simulation of a dipole measured in the presence of an infinite PEC back plane by using the method of images. Thus, Figure 15 and 16 contain false colour plots of the azimuth and elevation polarised electric field components that have been tabulated on a regular azimuth over elevation co-ordinate system, *c.f.* Figure 5 and 6 above which were forming from the linear superposition of the two dipole fields (originating from the real and virtual dipoles) with due regard to phase. From inspection of these figures it is evident that, as expected, the direct and reflected signals have combined constructively and destructively to form a complex, rapidly fluctuating, fringing pattern.

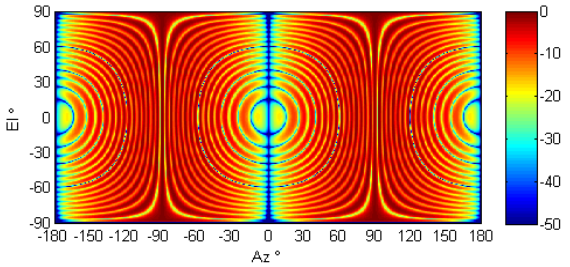

Fig. 15. E_{Az} Polarised far electric field component of Hertzian dipole in presence of PEC reflector.

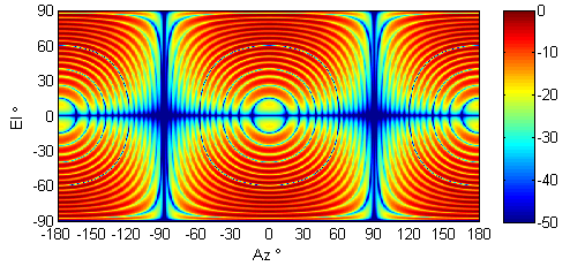

Fig. 16. E_{El} Polarised far electric field component of Hertzian dipole in presence of PEC reflector.

The equivalent mode plot can be seen presented in Figure 17 below. As expected, as the transforms are linear, Figure 17 can be seen to correspond closely with Figures 13 and 14 with the modes associated with the real Hertzian dipole being distributed narrowly at low values of n with modes associated with the virtual Hertzian dipole being distributed towards higher values of n thereby illustrating the mode orthogonalisation feature of the MARS measurement and post-processing. Although the virtual dipole has some influence on the lowest order modes, crucially, that influence is *circa* 70 dB below the contribution made by the real dipole. Thus, when the higher order modes are filtered out, the virtual dipole, *i.e.* the reflected indirect fields, will have *very* little influence on the resulting far-field pattern.

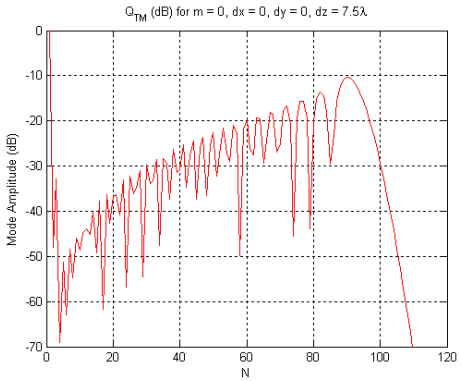

Fig. 17. Mode spectra for dipole in presence of PEC reflector located coaxially at $z = 7.5\lambda$ having been translated by -7.5λ to $z = 0$.

For the sake of completion, Figure 18 and 19 contain MARS processed far-field patterns that are directly comparable with the results presented in Figure 5 and 6 above. Here, the high angular frequency diffraction pattern that resulted from the PEC reflector can be seen to have been effectively supressed. A minor discrepancy can be observed at $Az = El = 0°$ which is a consequence of spherical mode leakage raising the noise floor in this direction. Use of a larger offset and a less aggressive filter function can ease this sort of minor artefact. Note that without the translation of origins, merely relying upon mode filtering alone will not produce the required result.

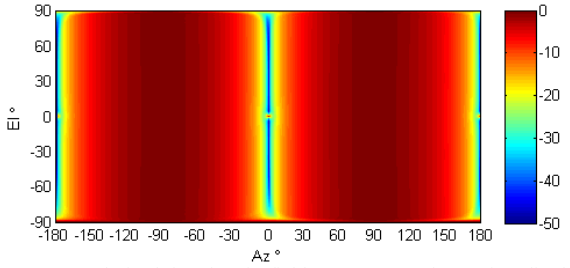

Fig. 18. E_{Az} Polarised far electric field component of Hertzian dipole with MARS processing.

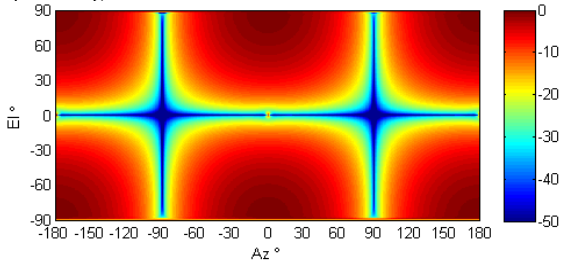

Fig. 19. E_{El} Polarised far electric field component of Hertzian dipole with MARS processing.

A further question which often arises which can also be illuminated through the use of this simulation concerns the accuracy and precision with which the translation is needed to be known. As with the effectiveness of the filtering itself, this is determined by the behaviour of the SMCs under the translation of origins. Equation 2 can be used to obtain a relationship between the displacement and the mode index. This follows from noting that when the mode index changes by unity, ρ_0 changes by $1/k_0$ thereby implying that providing the magnitude of the translation is specified to within $\pm 1/(2k_0)$, *i.e.* approximately 1/6 of a wavelength, this is sufficient to allow the mode spectra to be translated correctly. This can be seen

illustrated below in Figure 20 where the location of a single dipole has been changed by $1/k_0$ (*i.e.* 5 mm at 10 GHz) resulting in the mode spectra being translated by a single azimuthal mode index.

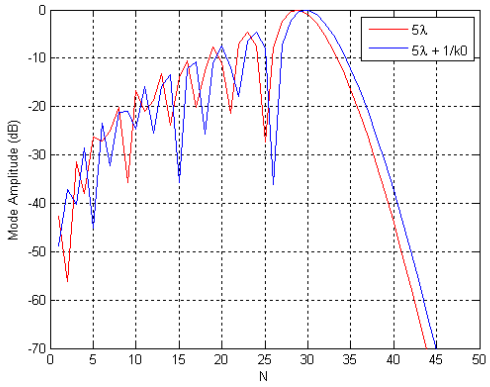

Fig. 20. Q_{TM} Mode spectra for M = 0 for dipole located coaxially at $z = 5\lambda$, and at $z = 5\lambda + 1/k_0$ showing one mode displacement of SMCs.

V. Summary And Conclusions

A simple, physical optics, based antenna measurement model that can be used to investigate the impact of various error terms within the facility level error budget of a given spherical near- or far-field range has been introduced. This model has been used to recreate a conventional S-MARS measurement whereupon similar phenomena have been observed in the CEM model as have been noted with actual range measurements. Specifically these are: 1) the effects of scattering on a far-field pattern depend upon the AUT displacement with larger displacements resulting in higher angular frequency ripple on the far-field patterns, 2) SMCs resulting from scattering are displaced to higher order modes, with AUT modes being displaced to lower order modes once the AUT is mathematically translated back to the origin of the measurement co-ordinate system, 3) the amount of separation between mode distributions associated with scattering and those associated with the AUT increases as the displacement increases, and 4) S-MARS is capable of effectively suppressing scattering providing the magnitude of the displacement is sufficiently large. This behaviour has also been observed when using cylindrical mode based expansions, *c.f.* [21].

As shown above, the CEM model has been able to provide further confirmation of the effectiveness of the S-MARS processing showing that it can be used with a very high degree of confidence. As can be seen from the overview present above since of all the stages used within the acquisition and post-processing are in common with the well-known and well understood principles of the SNF measurement theory, and all results to date have attested to the success of the method. The AUT displacement and the ensuing finer sample spacing are acceptable providing the sampling criterion is adhered to. The mathematical displacement of origins of the far-field data to the measurement origin is rigorous, with the selection of the mode filter being defined by the physical size of the antenna and its conceptually idealised measurement location. Finally, as this paper summarises the findings of an on-going programme of research the future plans include extending the simulation so that other more complex measurement configurations and experimental errors can be studied.

References

[1] G.E. Hindman, A.C. Newell, "Reflection Suppression in a large spherical near-field range", AMTA, Newport, RI, October. 2005.

[2] G.E. Hindman, A.C. Newell, "Reflection Suppression To Improve Anechoic Chamber Performance", AMTA Europe, Munich, Germany, March 2006.

[3] O.M. Bucci, G. D'Elia, M.D. Migliore, "A General and Effective Clutter Filtering Strategy in Near-Field Antenna Measurements", IEEE Proc.-Microwave Antennas and Propagation, Vol. 151, No. 3, June 2004.

[4] A.C. Newell, "Error Analysis Techniques for Planar Near-field Measurements", IEEE Transactions on Antennas and Propagation, vol. AP-36, pp. 754-768, June 1988.

[5] S.F. Gregson, A.C. Newell, G.E. Hindman, "Reflection Suppression In Cylindrical Near-Field Antenna Measurement Systems – Cylindrical MARS", AMTA, Salt Lake City, UT, November, 2009.

[6] S.F. Gregson, A.C. Newell, G.E. Hindman, M.J. Carey, "Extension of The Mathematical Absorber Reflection Suppression Technique To The Planar Near-Field Geometry", AMTA, Atlanta, October, 2010.

[7] S.F. Gregson, A.C. Newell, G.E. Hindman, P. Pelland, "Range Multipath Reduction In Plane-Polar Near-Field Antenna Measurements", AMTA, Seattle, October 2012.

[8] S.F. Gregson, B.M. Williams, G.F. Masters, A.C. Newell, G.E. Hindman, "Application of Mathematical Absorber Reflection Suppression To Direct Far-Field Antenna Range Measurements", AMTA, Denver, October 2011.

[9] S.F. Gregson, J. Dupuy, C.G. Parini, A.C. Newell, G.E. Hindman, "Application of Mathematical Absorber Reflection Suppression to Far-Field Antenna Testing", LAPC, Loughborough, November, 2011.

[10] S.F. Gregson, J. McCormick, B.J. Kerse, A.C. Newell, G.E. Hindman, "Computational and experimental verification of far-field mathematical absorber reflection suppression", 6th EuCAP, Prague, March, 2012.

[11] S.F. Gregson, A.C. Newell, G.E. Hindman, "Examination of Far-Field Mathematical Absorber Reflection Suppression Through Computational Electromagnetic Simulation", International Journal of Antennas and Propagation, Special Issue on Recent Advances in Near-Field to Far-Field Transformation Techniques, March 2012.

[12] Doren W. Hess, "The IsoFilter™ Technique: Isolating an Individual Radiator from Spherical Near-Field Data Measured in a Contaminated Environment", EuCAP 2007.

[13] F. Jensen, "On the probe compensation for near-field measurements on a sphere", Archiv für Elektronik und Übertragung-stechnik, Vol. 29, No. 7/8, 1975, pp. 305-308.

[14] J.E. Hansen, (Ed.), "Spherical Near-Field Antenna Measurements", Peter Peregrinus, Ltd., on behalf of IEE, 1988, London, UK.

[15] P.F. Wacker, "Near-field antenna measurements using a spherical scan: Efficient data reduction with probe correction", Conf. on Precision Electromagnetic Measurements, IEE Conf. Publ. No. 113, pp. 286-288, 1974, London, UK.

[16] H.C. Chen, "Theory of Electromagnetic Waves, A Coordinate-Free Approach", McGraw-Hill, 1983, ISBN 0-07-010688-6.

[17] J.M. Bowen, "A Study of Near-Field Sampling Grid Errors and Their Effect on Phased Array Beam-Pointing Error", AMTA Symposium, October, 2011.

[18] C.A. Balanis, "Advanced Engineering Electromagnetics", John Wiley & Sons, 1989, ISBN 0-471-62194-3.

[19] R.H. Clarke, J. Brown, "Diffraction Theory and Antennas", Ellis Horwood Ltd., 1980.

[20] S.F. Gregson, J. McCormick, C.G. Parini, "Principles of Planar Near-Field Antenna Measurements", The IET Technology, UK, 2007.

[21] S.F. Gregson, A.C Newell, G.E Hindman, M.J. Carey, "Advances in Cylindrical Mathematical Absorber Reflection Suppression", EuCAP, Barcelona, April, 2010.